Journal of
Synchrotron
Radiation
ISSN 0909-0495

Received 28 July 2006
Accepted 30 October 2006

An off-axis magnetron-sputtering system for *in situ* studies of artificial superlattices growth by synchrotron radiation scattering

Yuan-Chang Liang,[a] Hsin-Yi Lee,[b]* Heng-Jui Liu,[b] Yung-Wei Hsieh[b] and Yung-Ching Liang[b]

[a]Department of Mechanical Engineering, Chienkuo Technology University, Changhua 50094, Taiwan, and [b]National Synchrotron Radiation Research Center, 101 Hsin-Ann Road, Hsinchu Science Park, Hsinchu 30076, Taiwan. E-mail: hylee@nsrrc.org.tw

A sputtering chamber for the growth of artificial superlattices of oxide-based materials is described. The chamber is designed to fit into a standard Huber eight-circle diffractometer. The chamber serves for investigation with synchrotron radiation of growth characteristics of oxide-based artificial superlattices *in situ*. Two Be windows of large area in the vacuum chamber enable measurement of reflections of X-rays at entrance and exit angles up to $\sim 50^{\circ}$. Large perpendicular momentum transfers are practical with this apparatus. The possibility of investigating X-ray scattering *in situ* is demonstrated by observation of the effects of the modulation length and the stacking period on the growth characteristics of $BaTiO_3/LaNiO_3$ artificial superlattices.

© 2007 International Union of Crystallography
Printed in Singapore – all rights reserved

Keywords: X-ray diffraction; X-ray reflectivity; artificial superlattices; RF sputtering.

1. Introduction

Artificial superlattices of perovskite oxides receive much attention owing to their novel physical properties that differ from those of their constituent compounds (Kim *et al.*, 2003; Christen *et al.*, 1998; Ueda *et al.*, 1998). For instance, studies of superlattice structures with perovskite-based manganites have revealed interesting magnetic properties such as an exchange-bias effect (Panagiotopoulos *et al.*, 1999) and anti-ferromagnetic interlayer coupling (Nikolaev *et al.*, 1999). In work on $BaTiO_3/LaNiO_3$ (BTO/LNO) superlattices, we observed a significant dielectric enhancement, attributed to the large lattice strain induced in the heteroepitaxial superlattices (Liang *et al.*, 2004). In a rigorous investigation of the properties of artificial superlattices, it is important to characterize their crystal structures in detail. For a superlattice structure, lateral lattice matching between heteroepitaxial compounds occurs up to only a critical thickness, beyond which misfit dislocations are generated at the interface to compensate for the accumulated lattice strain. Investigation of the characteristics of lattices in the growth of an epitaxic superlattice is therefore important for the preparation of perovskite oxide superlattices with nanometer modulation lengths, and clarification of the evolution of surface and interface morphology is a challenging aspect of these superlattice materials. The presence of interfacial roughness and strain is inevitable during the formation of a boundary between two media. The mechanism of multilayer growth is associated with the evolution of the roughness at the interface and its nature along the whole stack of the multilayer. X-ray diffraction is an appropriate technique for studying the structure of superlattices as their structures are characterized by satellite peaks around the main Bragg peak of the averaged lattice. X-ray reflectivity has been demonstrated to be a powerful non-destructive technique for studying the structure of the buried interface and the surface morphology. The combination of X-ray diffraction and reflectivity provides a powerful approach to characterizing structural information of superlattices (Fullerton *et al.*, 1993; He *et al.*, 1992). Because of the non-equilibrium situation, measurement *in situ* makes it easier to extract a consistent physical description of the system from the data. Real-time characterization using X-rays from synchrotron radiation is especially useful in this research field (Fullerton *et al.*, 1993; Lee *et al.*, 2000; Zimmermann *et al.*, 1998; Kang & Je, 2002; Stephenson *et al.*, 1999; Matz *et al.*, 2001; Bøttiger *et al.*, 2002). Various growth techniques, such as molecular-beam epitaxy (MBE) and pulsed-laser deposition (PLD), have been used to grow superlattice films of complex oxides. Both PLD and MBE bestow the advantages of maintaining control of stoichiometry, crystal structure, crystal orientation *etc.* In view of compatibility with industrial fabrication, the growth of a superlattice film by radio-frequency (RF) magnetron-sputtering deposition is highly desirable. In this work we constructed a sputtering chamber that is

doi:10.1107/S0909049506045304

mounted on a standard Huber eight-circle diffractometer for study *in situ* of the growth characteristics of artificial superlattices of perovskite oxides.

2. Design criteria and description of the chamber

To derive structural information about a superlattice film *in situ*, the related X-ray scattering methods should involve at least the measurements of X-ray reflectivity to determine the sublayer electron density, surface and interface roughnesses, and film thickness, and measurements of wide-angle crystal-truncation-rod (CTR) scattering to determine the lattice parameters and crystalline quality. To control the alternating stack of separate compounds *in situ*, two RF sputtering guns equipped with two computer-controlled shutters, one for the target and the other for the sample, are required to be present in the vacuum chamber. For the growth of epitaxic perovskite oxides, single-crystal substrates such as $SrTiO_3$, $LaAlO_3$ and MgO are widely adopted. The position of the (002) Bragg diffraction of these substrates using 10 keV synchrotron radiation is 2θ = 37.01° for $SrTiO_3$, 38.17° for $LaAlO_3$ and 34.23° for MgO, and using 8 keV synchrotron radiation is 2θ = 46.37° for $SrTiO_3$, 48.25° for $LaAlO_3$ and 43.17° for MgO. The aperture size of beryllium windows for X-ray incidence and exit should thus be carefully designed to meet the wide-angle diffraction requirement during use of these substrates for the epitaxic growth of superlattices. Another important factor in the fabrication of high-quality epitaxic superlattices is the substrate temperature: a temperature of at least 773 K is believed to be necessary for the growth of an epitaxic oxide using the RF sputtering technique (Liang *et al.*, 2004).

The chamber for sputtering *in situ* has three parts as shown in Fig. 1. The upper part is a hollow cylinder with one bottom opening (diameter 150 mm) that is equipped with two flanges for RF-magnetron sputtering guns, one gas inlet and two feedthroughs for shutters on top of the chamber. Two rectangular flanges are located on the circumference of the cylinder chamber for beryllium windows, with an outer area of 140 mm × 120 mm and an aperture area of 100 mm × 80 mm. This condition allows the X-ray detector to detect the diffraction intensity in the vertical scattering plane at an angle of 50° that is suitable for most single-crystal substrates for the epitaxic growth of perovskite oxides. There is also a CF flange (70 mm) for a view port and a VCR flange for an absolute pressure transducer (MKS Baratron type 626A). To avoid high temperatures caused by the plasma and the substrate, two cooling-water channels are placed inside the top and bottom metal walls of the chamber. Inside the chamber, aluminium foil (thickness 0.02 mm) surrounds the inner wall to keep thermal radiation and sputtering contamination off the beryllium windows during deposition of a thin film. Two flanges for sputtering guns are tilted 24° away from the normal direction, and are equipped with balanced RF magnetron guns (AJA International, model ST10). Sputtering guns are focused on the substrate at a distance of 100 mm from the target surface to the substrate surface. The target has a thickness of 3 mm and a diameter of 25.4 mm. Additionally, each sputtering gun is equipped with a gas ring chimney to concentrate the plasma and to prevent cross-contamination from the other target. Two pneumatically controlled shutters are placed in front of the chimney and the substrate; they are remotely controlled using PLC (programmable logical controller) systems from a computer station outside the experimental hutch. Thereby we control precisely the duration of deposition of each layer during the deposition of a superlattice. As shown in Fig. 2, the upper shutter is normal to the target surface at a distance of 24 mm, and can rotate 180° to the other side for use of the other sputtering gun. The lower shutter is just on the substrate at a distance of 50 mm, and can rotate 90° to leave the substrate surface during sputtering. A feedthrough (Swagelok) serves for the gas inlet to allow Ar and O_2 mixed gas into the chamber at the required working pressure. The mixed gas enters *via* individual channels of Ar and O_2 and are then combined with a fitting (Union Tee).

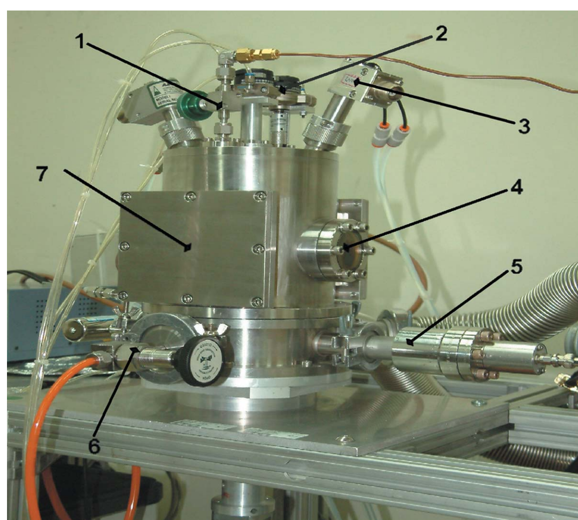

Figure 1
Photograph of the deposition chamber: (1) feedthrough for gas inlet (to allow mixed Ar and O_2 gases into the chamber), (2) pneumatically controlled shutter, (3) sputtering gun, (4) view port, (5) cold-cathode gauge, (6) needle valve to lead pure N_2 gas to break the vacuum, (7) Be window port.

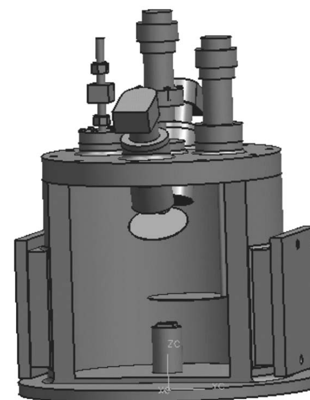

Figure 2
Cross section with interior view of the sputtering deposition chamber.

The middle part is also a cylinder that can be connected onto the φ circle of the Huber eight-circle X-ray diffractometer. This part has four NW40 and two NW25 ports on the circumference. One of these four NW40 ports is for a turbomolecular pump (SEIKO SEIKI) and a molecular drag pump (MDP, Alcatel Drytel 31); they are connected *via* bellows and a throttle valve. A second port is for a gas inlet (needle valve) leading pure N_2 gas into the vacuum chamber, a third for electrical feedthrough of a thermocouple and heater-conducting wires, and a fourth is blanked. One of two NW25 ports is for a convectron gauge (Granville-Phillips), and the other is for a high-vacuum cold-cathode gauge.

The lowest part of the chamber contains a sample stage equipped with motorized rotary and linear motion controlled by a stepper motor, to allow fine adjustment of the orientation and height of a sample to the center of the incident X-ray beam. Inside the part underneath, the sample stage is equipped with a heater (Heatwave Laboratories model 101491) composed of a resistance covered with a ceramic carrier and a heat shield; this heater is also equipped with three sample clips to fix the sample. The K-type thermocouple is placed inside the shield and is in contact with the ceramic block. The ceramic carrier has a diameter of 25.4 mm, allowing a sample size of 10 mm $\times$ 10 mm in our experiment. The temperature of the sample surface can reach 1273 K in operation with O_2. The temperature of the sample was measured using a thermocouple in contact with the substrate. The total mass of the chamber is about 16 kg, which allows for the standard Huber eight-circle diffractometer having a vertical load of 40–50 kg and a side load of ~15 kg. The entire sputtering chamber is mounted on the Φ-circle of the diffractometer and can be moved with the χ-circle. The azimuthal axis of the sample stage is aligned with the φ axis. The samples stage is equipped with a motorized rotary that allows the sample to be rotated freely without rotating the entire sputtering chamber during scattering measurements. This arrangement allows us to conduct in-plane scattering experiments *in situ* during film growth.

The chamber can attain a basic pressure of 1×10^{-6} torr, and all sputtering is automatically controllable by computer. For the deposition of a superlattice, we set the time for the required thickness of each material, the delay for the lower shutter and the required periods on the computer, and then input these parameters into the PLC control system. Before deposition, the lower shutter remains above the substrate and the upper shutter in front of one of the guns (as illustrated in Fig. 2). When the sputtering deposition begins, the lower shutter is moved so as to expose the substrate to bathe in the plasma of the gun without a shutter in front. When this material is deposited for the designated duration of deposition, the lower shutter returns to a position above the substrate and remains there for the designated delay. After that, the upper shutter rotates 180° to the other side and the lower shutter rotates to leave the sample in turn. The second material is deposited onto the first deposited material. By repeating this deposition, we obtain a superlattice film with the expected sublayer thickness and period.

3. Example of a test experiment: *in situ* X-ray scattering during crystal growth of symmetric $BaTiO_3/LaNiO_3$ superlattices

Deposition was performed at sputtering power densities of 3.95 and 2.96 W cm^{-2} for BTO and LNO, respectively. During deposition, the substrate temperature was maintained at 773 K; the working pressure of deposition was fixed at 30 mtorr with an Ar/O_2 ratio of 4:1. The rate of deposition of a BTO and LNO film is 0.5 nm min^{-1}, estimated from the X-ray reflectivity curves. The synchrotron X-ray scattering experiments were performed at wiggler beamline BL-17B1 at the National Synchrotron Radiation Research Center, Taiwan. The experimental set-up is shown in Fig. 3. The incident X-rays were focused vertically with a mirror and monochromated to an energy of 10 keV using a Si(111) double-crystal monochromator. With two pairs of slits between the sample and the detector, the typical wavevector resolution in the vertical scattering plane was set to ~0.005 nm^{-1} in this experiment.

First, we examined the effect of the constituent sublayer thickness on the evolution *in situ* of the surface and interface structure in the initial stages of growth of BTO/LNO superlattices. The designated thickness of a sublayer was fixed at 1, 3 and 10 nm. A symmetric sublayer structure, *i.e.* $(BTO_m/LNO_m)_n$ in which m is the thickness of a sublayer in nm and n is the number of bilayers, was adopted. Fig. 4 shows the specular component of the X-ray reflectivity *in situ* against momentum transfer (q_z) in reciprocal space along the normal direction of the substrate surface obtained from a superlattice with varied sublayer thickness and number of bilayers. The principle of X-ray reflectivity is based on the recursive formalism of Parratt (1954). In this work we fitted the reflectivity data with the Bede *REFS Mercury* code (Bowen & Tanner, 1974) to determine the physical parameters of the superlattice, such as roughness, thickness and density. This program calculates the reflectivity of the material using the dynamical

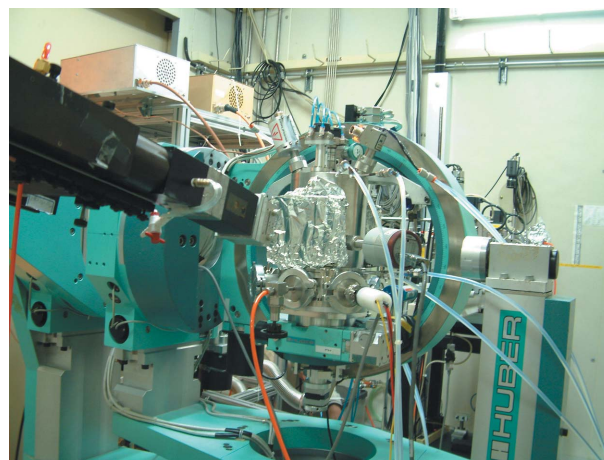

Figure 3
Photograph of the deposition chamber mounted into a standard Huber eight-circle diffractometer. The rectangular flanges covered with aluminium foil are for the assembly of the Be windows.

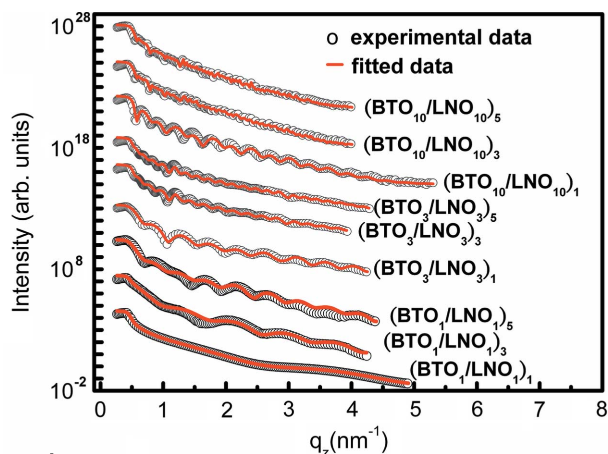

Figure 4
Curves for specular X-ray reflectivity *in situ* for BTO/LNO superlattices with varied modulation lengths and stacking periods.

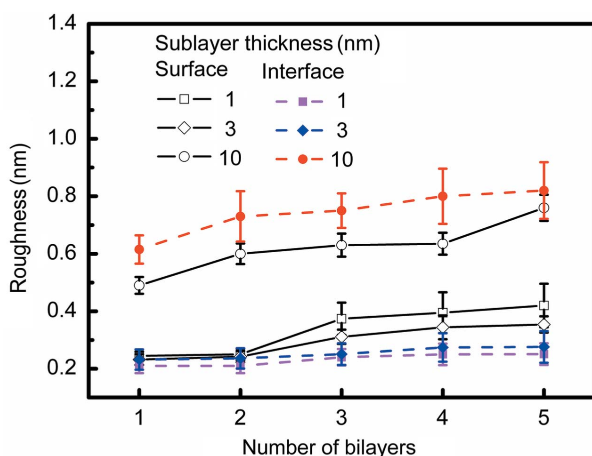

Figure 5
Evolution of surface and interface roughnesses of superlattices in the initial stage of growth. The sublayer thickness was fixed at 1, 3 and 10 nm and the bilayer number varied from 1 to 5. The data were derived from the fitting results of curves of X-ray reflectivity *in situ*.

Fresnel equations for multilayer reflectivity, taking account of absorption, instrumental resolution, interface roughness and abruptness, and sample curvature (Bowen & Tanner, 1974). In each curve the diffuse scattering was first subtracted so that the data points (open circles) represented only the specular component. The intensity oscillation originates from the interference of X-rays reflected from the growing surface and those reflected from the interfaces of separate constituent compounds and the film/STO substrate (Zimmermann *et al.*, 1998). Fig. 4 shows clearly the presence of well defined Kiessig fringes that clearly reveal the presence of a well ordered layer structure for a series of superlattices. The thickness of the film is given by $2\pi/\Delta q_z$ (van der Lee, 2000), in which Δq_z is the period of the oscillation. Hence, the period of oscillations becomes denser as the thickness of the stacking period or the number of bilayers increases.

For a BTO/LNO superlattice, the lattice mismatch in this system is estimated to be $\sim$3%; this large misfit will make the lateral coherent growth of constituent compounds just up to a few modulation lengths. According to the

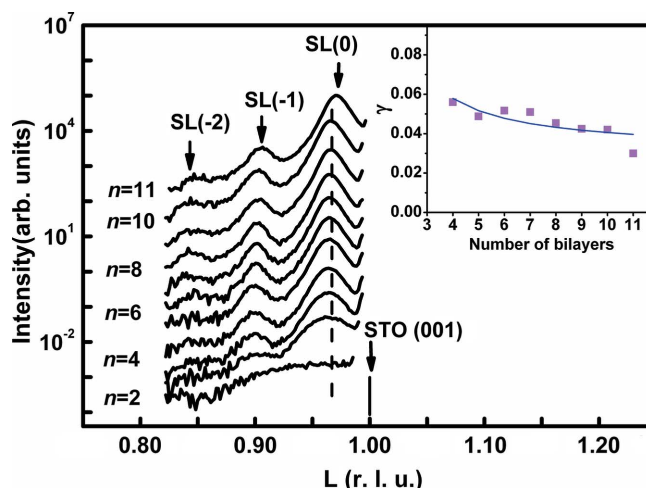

Figure 6
(00L) CTR intensities of a $(BTO_{3\,nm}/LNO_{3\,nm})_n$ superlattice grown *in situ* on a STO (001) substrate with varied stacking period (n). The inset shows the values of the γ factor, *i.e.* $(I_{sat} - I_{back})/(I_0 - I_{back})$, as a function of bilayer number.

Matthews–Blakeslee theory (Matthews & Blakeslee, 1974), the critical modulation length is estimated to be more than 16 nm. The oscillation amplitude of X-ray reflectivity curves decays exponentially, corresponding to the relation $\exp[-q_z^2(\sigma_s^2 + \sigma_i^2)/2]$, in which σ_s is the roughness of the surface, σ_i is that of the interface, and q_z is the momentum transfer normal to the sample surface (Noh *et al.*, 1995). Fig. 5 summarizes the evolution *in situ* of the surface and interface roughnesses from superlattices against bilayer number. From the multilayer stack with a sublayer thickness of 3 nm and between bilayers numbering 1–5, the surface and interface roughness are maintained at about 0.28 nm (surface roughness $\sim$0.25 nm for the bare STO substrate); this condition might be a consequence of the repetition of the two-dimensional nucleation and growth of the BTO and LNO sublayers on the flat terrace of the STO substrate, as proposed by Visinoiu *et al.* (2002). As the sublayer thickness increases further to 10 nm, larger than the critical thickness, the surface and interface roughnesses increase greatly, through the relief of strain in the multilayer stack. The interface roughness seems to be notably larger than that of the surface for a sublayer thickness of 10 nm and bilayers numbering 1–5. According to the mechanism of strain relief in heteroepitaxy (Sun *et al.*, 2004), the dislocation half-loop generally nucleates at the film surface, resulting in a surface undulation, and then extends towards the interface. More half-loops might meet and combine to form a long straight-edge dislocation line at the interface, which helps to relax the misfit strain. Hence, a high density of misfit dislocations appears at the BTO/LNO interface and seriously deteriorates the interface structure.

In general, the strain state of a superlattice depends on the elastic properties of the constituent compounds; moreover, the total thickness of the superlattice has also a profound effect on the degree of strain in the superlattice even though the sublayer thickness is less than the critical value (Liang *et al.*, 2004). Fig. 6 shows the evolution of (001) CTR spectra of a

superlattice with increasing numbers of BTO/LNO bilayers. The sublayer thickness of each compound is fixed at 3 nm, which is below the theoretical critical value as discussed above. For simplicity, values of H, K and L specified in this paper are expressed in reciprocal lattice units (r.l.u.) referred to the STO lattice parameter (0.3905 nm near 295 K). The satellite peaks adjacent to the zero-order peak are observed to arise from the chemical modulation of the multilayer structure. The intensity of CTR spectra for the zero-order peak increases with increasing number of stacks. Moreover, as shown in Fig. 6, the zero-order peak, SL(0), of a superlattice with bilayers numbering 11 shows a small but distinct shift towards a greater L-index, indicating the occurrence of a large strain relaxation in the superlattice (Peng *et al.*, 2003). This observation is consistent with the result of a factor, defined as $(I_{\rm sat} - I_{\rm back})/(I_0 - I_{\rm back})$, in which $I_{\rm sat}$ is the intensity of a first-order satellite peak at smaller angle, I_0 is the intensity of a zero-order peak, and $I_{\rm back}$ is the background intensity (Flevaris *et al.*, 1981). As illustrated in the inset of Fig. 6, this factor decreases markedly at bilayers numbering 11; this decrease indicates a greatly increased interfacial roughness in association with the onset of structural relaxation at the BTO/LNO hetero-interface through the formation of misfit dislocations (Kano *et al.*, 1993).

Fig. 7 summarizes the evolution of the interfacial and surface roughnesses against the number of bilayers obtained from best fits of the data for specular reflectivity *in situ*. The interfacial and surface roughnesses of bilayers numbering 9 increase only insignificantly from those of a bare STO substrate (~0.25 nm). An increase of surface and interfacial roughnesses clearly occurs at bilayers numbering 10. An undulated surface has a larger surface area and thus a greater surface energy, which is compensated by a decreased strain energy near the film surface (Xie *et al.*, 1994). An abruptly increased surface roughness at bilayers numbering 10 might result from this effect. On further increase of bilayers numbering 11, the interfacial roughness increases greatly, apparently related to the relief of lattice strain in the superlattice. This result conforms well to that from the inset of Fig. 6. Although there is no measurable shift of zero-order peak at bilayers numbering 10 in the CTR intensity profiles, probably because strain relief is too small to be observable (Dodson & Tsao, 1987; Fritz, 1987), according to both diffraction and specular reflectivity results the onset of strain relaxation is likely to occur at bilayers numbering 10–11. This stage corresponds to the effective thickness beyond which surface and interface undulation results from the generation of misfit dislocations in the superlattice.

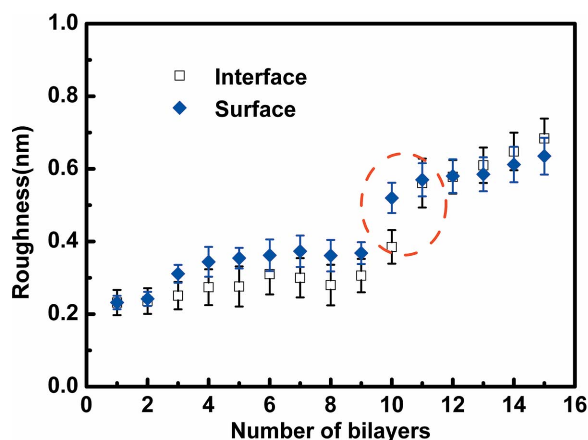

Figure 7
Evolution of surface and interface roughnesses deduced from the fitting results of curves of X-ray reflectivity *in situ* of a $(\mathrm{BTO}_{3\,\mathrm{nm}}/\mathrm{LNO}_{3\,\mathrm{nm}})_n$ superlattice as a function of bilayer number. The circle region shows the abruptly increased surface and interface roughnesses occurring at 10–11 bilayers.

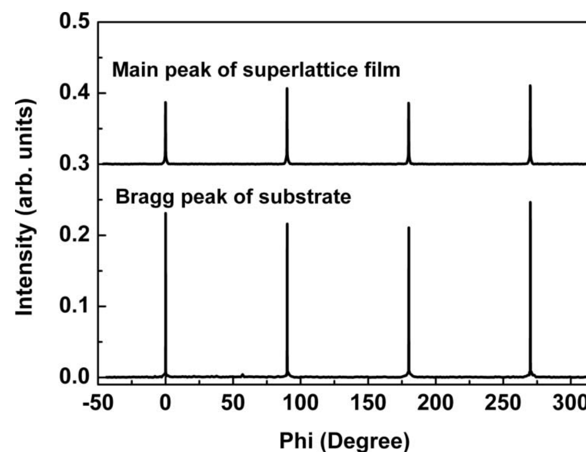

Figure 8
X-ray azimuthal scan of the (101) substrate Bragg peak and main peak for a $(\mathrm{BTO}_{3\,\mathrm{nm}}/\mathrm{LNO}_{3\,\mathrm{nm}})_{10}$ superlattice film.

We also investigated the epitaxic relation between the BTO and LNO layers in the superlattices by examining in-plane (101) Bragg peaks of the superlattice films. The azimuthal diffraction patterns of the $(\mathrm{BTO}_{3\,\mathrm{nm}}/\mathrm{LNO}_{3\,\mathrm{nm}})_{10}$ superlattice film in the vicinity of a main peak and substrate Bragg peak clearly exhibiting a fourfold symmetry with the same orientation appear in Fig. 8. These results constitute firm evidence for strong epitaxy of the deposited layer on the substrate. No other peaks are observed in the intervals between the four peaks, indicating a perfect alignment of a and c axes of BTO and LNO strained unit cells along those of the STO substrate.

4. Conclusions

We have described a sputtering system for the study of the growth of artificial superlattices of oxide-based materials using synchrotron radiation. The chamber is mounted on a standard Huber eight-circle diffractometer. X-ray reflectivity *in situ* directly reveals the correlation between the sublayer thickness and the growth mechanism of the superlattice, *i.e.* fully strained growth layer by layer or strained relief island growth. A combination of X-ray diffraction and reflectivity provides a valuable method of characterizing the effective total thickness of a superlattice with a fixed sublayer thickness. This apparatus is suitable for the investigation *in situ* of most artificial superlattice materials with synchrotron radiation.

The National Science Council of the Republic of China provided support under contracts NSC 94-2218-E-270-002 and NSC 94-2216-E-213-001.

References

Bøttiger, J., Chevallier, J., Petersen, J. H., Schell, N., Matz, W. & Mücklich, A. (2002). *J. Appl. Phys.* **91**, 5429–5433.
Bowen, D. K. & Tanner, B. K. (1993). *Nanotechnology*, **4**, 175–182.
Christen, H. M., Specht, E. D., Norton, D. P., Chisholm, M. F. & Boatner, L. A. (1998). *Appl. Phys. Lett.* **72**, 2535–2537.
Dodson, B. W. & Tsao, J. Y. (1987). *Appl. Phys. Lett.* **51**, 1325–1327.
Flevaris, N. K., Baral, D., Hilliard, J. E. & Ketterson, J. B. (1981). *Appl. Phys. Lett.* **38**, 992–994.
Fritz, I. J. (1987). *Appl. Phys. Lett.* **51**, 1080–1082.
Fullerton, E. E., Pearsion, J., Sowers, C. H. & Bader, S. D. (1993). *Phys. Rev. B*, **48**, 17432–17444.
He, Y. L., Yang, N. H., Lu, T. M. & Wang, G. C. (1992). *Phys. Rev. Lett.* **69**, 3770–3773.
Kang, T. S. & Je, J. H. (2002). *Appl. Phys. Lett.* **80**, 1361–1363.
Kano, H., Kagawa, K., Suzuki, A., Okabe, A., Hayashi, K. & Aso, K. (1993). *Appl. Phys. Lett.* **63**, 2839–2841.
Kim, L., Jung, D., Kim, J., Kim, Y. S. & Lee, J. (2003). *Appl. Phys. Lett.* **82**, 2118–2120.
Lee, A. van der (2000). *Solid State Sci.* **2**, 257–278.
Lee, H. Y., Liang, K. S., Lee, C. H. & Wu, T. B. (2000). *J. Mater. Res.* **15**, 2606–2611.
Liang, Y. C., Wu, T. B., Lee, H. Y. & Hsieh, Y. W. (2004). *J. Appl. Phys.* **96**, 584–589.
Matthews, J. W. & Blakeslee, A. E. (1974). *J. Cryst. Growth*, **27**, 118–125.
Matz, W., Schell, N., Neumann, W., Bøttiger, J. & Chevallier, J. (2001). *Rev. Sci. Instrum.* **72**, 3344–3348.
Nikolaev, K. R., Bhattacharya, A., Kraus, P. A., Vasko, V. A., Cooley, W. K. & Goldman, A. M. (1999). *Appl. Phys. Lett.* **75**, 118–120.
Noh, D. Y., Hwu Y., Kim, H. K. & Hong, M. (1995). *Phys. Rev. B*, **51**, 4441–4448.
Panagiotopoulos, I., Christides, C., Pissas, M. & Niarchos, D. (1999). *Phys. Rev. B*, **60**, 485–491.
Parratt, L. G. (1954). *Phys. Rev.* **95**, 359–369.
Peng, L. S.-J., Xi, X. X., Moeckly, B. H. & Alpay, S. P. (2003). *Appl. Phys. Lett.* **83**, 4592–4594.
Stephenson, G. B., Eastman, J. A., Auciello, O., Munkholm, A., Thompson, C., Fuoss, P. H., Fini, P., DenBaars, S. P. & Speck, J. S. (1999). *Mater. Res. Soc. Bull.* **24**, 21–25.
Sun, H. P., Tian W., Pan, X. Q., Haeni, J. H. & Schlom, D. G. (2004). *Appl. Phys. Lett.* **84**, 3298–3300.
Ueda, K., Tabata, H. & Kawai, T. (1998). *Science*, **280**, 1064–1066.
Visinoiu, A., Alexe, M., Lee H. N., Zakharov, D. N., Pignolet, A., Hesse, D. & Gosele, U. (2002). *J. Appl. Phys.* **91**, 10157–10162.
Xie, Y. H., Gilmer, G. H., Roland, C., Silverman, P. J., Buratto, S. K., Cheng, J. Y., Fitzgerald, E. A., Kortan, A. R., Schuppler, S., Marcus, M. A. & Citrin, P. H. (1994). *Phys. Rev. Lett.* **73**, 3006–3009.
Zimmermann, U., Schlomka, J.-P., Tolan, M., Stettner, J., Press, W., Hacke, M. & Mantl, S. (1998). *J. Appl. Phys.* **83**, 5823–5830.